INTERNATIONAL JOURNAL FOR NUMERICAL METHODS IN ENGINEERING
Int. J. Numer. Meth. Engng 2007; **71**:583–605
Published online 11 January 2007 in Wiley InterScience (www.interscience.wiley.com). DOI: 10.1002/nme.1981

Implementation aspects of the bridging scale method and application to intersonic crack propagation

David E. Farrell[1], Harold S. Park[2] and Wing Kam Liu[1,*,†]

[1]*Department of Mechanical Engineering, 2145 N. Sheridan Rd., Northwestern University, Evanston, IL 60208 3111, U.S.A.*
[2]*Department of Civil and Environmental Engineering, Vanderbilt University, Nashville, TN 37235, U.S.A.*

SUMMARY

The major purpose of this work is to investigate the performance of the bridging scale method (BSM), a multiscale simulation framework for the dynamic, concurrent coupling of atomistics to continua, in capturing shear-dominant failure. The shear-dominant failure process considered in this work is intersonic crack propagation along a weak plane in an elastic material, similar to the seminal molecular dynamics (MD) simulations by Abraham and Gao (*Phys. Rev. Lett*. 2000; **84**(14):3113–3116). We show that the BSM simulations accurately capture the essential physics of the intersonic crack propagation, including the formation of a daughter crack and the sudden acceleration of the crack to a velocity exceeding the material shear wave speed. It is also demonstrated that the non-reflecting boundary condition can adequately dissipate the strongly localized wave formed by the Mach cone after the crack accelerates beyond the material shear wave speed. Finally, we provide the algorithm for our implementation of the BSM, as well as the code used to determine the damping kernels *via* a newly adopted technique which is less expensive than previous methods. Copyright © 2007 John Wiley & Sons, Ltd.

Received 22 January 2006; Revised 1 December 2006; Accepted 6 December 2006

KEY WORDS: bridging scale; intersonic crack; concurrent coupling; implementation; multiple scale

1. INTRODUCTION

In the last decade, great effort has been put forth to develop simulation methods which can resolve material behaviour across the multiple length scales present in many physical systems. The bulk

*Correspondence to: Wing Kam Liu, Department of Mechanical Engineering, 2145 N. Sheridan Rd., Northwestern University, Evanston, IL 60208 3111, U.S.A.
†E-mail: w-liu@northwestern.edu

Contract/grant sponsor: NSF
Contract/grant sponsor: NSF IGERT Program
Contract/grant sponsor: NSF-Navy Civilian Service Fellowship Program
Contract/grant sponsor: Army Research Office

of this work has been motivated by new design paradigms that require an understanding of the phenomena at the continuum level brought on by the underlying micro- or nanoscale physics, for applications such as MEMS/NEMS devices or novel alloy design. Recently, attention has also been directed towards biological systems, many of which exhibit a strongly coupled hierarchical nature. In systems design, the traditional engineering simulation approach has made extensive use of continuum level modelling *via* empirical constitutive relations and numerical methods such as the finite element method (FEM) [1, 2], while atomistic level methods such as molecular dynamics (MD) [3, 4] have been used to study detailed phenomena such as dislocation nucleation and propagation or the details of failure mechanisms. Each of these approaches has limitations: in the case of FEM, the resolution is limited to the size of the continuum element for which the constitutive relation employed remains valid. For MD, the enormous number of degrees of freedom required for a continuum level simulation makes its use intractable for system sizes greater than hundred of nanometers. Thus, it is desirable to seek a method which can be used over large length scales, but maintain atomistic or near-atomistic resolution in regions of interest.

A number of multiple-scale methods have been proposed to bridge the gap between the disparate continuum and atomistic length scales. One method, based on an adaptive FEM approach, is the quasicontinuum method of Tadmor and co-workers [5, 6]. Other approaches have sought to couple continuum and atomistic simulations directly, such as the bridging domain method [7], the molecular atomistic *ab initio* dynamics method (MAAD) [8, 9], the dynamic coupling work of E and co-workers [10, 11], the multigrid approach of Fish and co-workers [12], and recent work on finite temperature effects in coupled atomistics/discrete dislocation (CADD) methods [13, 14]. Efforts are also underway by Oden and co-workers [15] to investigate reliability and error estimation for multiple-scale methods. Further, work on the consistency of atomic stress definitions has been performed by Zhou [16, 17] as well as Zimmerman and co-workers [18]. For additional detail, we refer the interested reader to available reviews on multiple-scale methods including those by Curtin and Miller [19] and Liu and co-workers [20, 21]. The remainder of this paper, however, will focus on the bridging scale method (BSM) of Liu and co-workers [22–27], which was developed as a framework for the dynamic, concurrent coupling of atomistics and continua.

The phenomena under consideration in this paper is the intersonic crack propagation (sometimes referred to as transonic). Based on continuum fracture mechanics, mode II cracks can propagate in two regimes based on crack-tip velocity [28]. The first of these regimes corresponds to crack-tip velocities lower than the Rayleigh wave speed, c_R, which is also the maximum velocity for mode I cracks. The second regime corresponds to crack-tip velocities faster than the material shear wave speed, c_s, but less than the material longitudinal wave speed, c_l; this regime is referred to as the *intersonic* regime [28, 29]. For velocities between the Rayleigh wave speed and the shear wave speed, the stress state ahead of the crack tip becomes compressive, and thus the crack cannot propagate [28]. These velocity regimes are illustrated in Figure 1.

We shall not provide an exhaustive review of the literature with respect to intersonic crack propagation, as the object of this work is to demonstrate the abilities of the BSM. With this in mind, the authors feel that it is important to note the experimental studies of Rosakis and co-workers [30] and acknowledge the continuum simulations which have been performed, such as those of Liu and co-workers [31–33]. Due to the nature of the present work, the MD and corresponding continuum analysis by Abraham and co-workers as presented in [34, 35] is also quite relevant. In their work, they studied the shear dominant fracture of a perfectly elastic body, in which an initial edge crack propagated along a weak plane of atoms at the centreline of the material. They performed MD simulations using a nearest neighbour harmonic potential to represent

DOI: 10.1002/nme

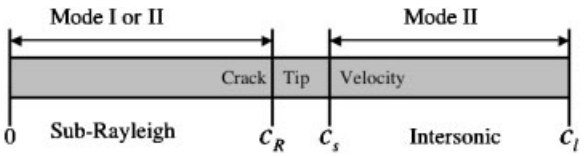

Figure 1. Schematic of crack-tip velocity regimes. There exists a 'forbidden' velocity region for Mode II cracks between the Rayleigh wave speed, c_R and material shear wave speed, c_s. The upper limit is near the material longitudinal wave speed, c_l.

the perfectly elastic body, and a nearest neighbour Lennard-Jones potential to represent the weak plane. They noted that in agreement with analytical studies and experiments, the crack-tip velocity underwent a transition from the Rayleigh wave speed to the longitudinal wave speed, due to the formation of a daughter crack ahead of the main crack tip and its subsequent acceleration. They also discussed that the daughter crack was not an intersonic dislocation as it had a well-defined opening which was visible during the simulation. Further, while the basic mechanism of fracture, i.e. the formation of a daughter crack and subsequent acceleration of the main crack, agreed with the continuum analysis, the MD simulation displayed distinct asymmetry at the crack tip, attributed to the anharmonic interactions present in the weak plane.

The phenomenon of intersonic crack propagation contains some interesting physical features, such as the formation of a Mach cone at the leading edge of the crack only after the crack-tip velocity exceeds the shear wave speed. To the authors' knowledge, the BSM has not been applied to a problem that includes shear dominant loading, crack speeds in the intersonic regime or shock-type wave propagation due to the presence of a Mach cone in the body. Thus, in addition to being able to further investigate the mechanism of crack-tip acceleration, we seek to study the dissipative abilities of the BSM interface and the performance of the BSM in shear dominant loading.

The outline of the paper is as follows. We shall first provide a brief overview of the BSM. The formulation to be discussed is the so-called displacement formulation presented by Park *et al*. [36] as well as Tang *et al*. [23], both of which are based on the work of Wagner and Liu [22]. Next we provide a discussion on the algorithm and methodology of the implementation, including the newly adopted method for determining the damping kernels. We then provide the problem description and results for the intersonic fracture simulations we have performed. Finally, we present in the appendices the algorithm used in the BSM implementation as well as the code used to determine the damping kernels for the lattice structure and interatomic potential considered in this work.

2. FORMULATION

The BSM was originally developed as a framework for coupling atomistic and continuum simulations. In particular, it was developed to dynamically and concurrently couple MD and FEM simulations. In this section, we will focus on the displacement formulation of Park *et al*. [36], based on the work of Wagner and Liu [22]. This presentation will also draw from the mathematically rigorous derivation presented by Tang *et al*. [23]. We present only a brief discussion and the final equations, and refer the interested reader to [22–27] for detailed derivations.

DOI: 10.1002/nme

The derivations in [22, 23] both consider a body similar to that in Figure 2. The derivation has three key points:

(1) The total displacement $\mathbf{u}$ in a domain Ω may be decomposed into coarse scale ($\bar{\mathbf{u}}$) and fine scale ($\mathbf{u}'$) parts

$$\mathbf{u} = \bar{\mathbf{u}} + \mathbf{u}' \tag{1}$$

(2) The total displacement $\mathbf{u}$ in Ω is described by MD. We define a coarse scale basis throughout Ω which co-exists with the MD, as illustrated in Figure 2(a). The course scale will be represented by FEM, with nodal displacements $\mathbf{d}$.
(3) In order to reduce the expense of the simulation, we eliminate the calculations which contain fine scale information (i.e. the MD) from the subregion Ω_C. This is done through the application of linear lattice mechanics principles at the interface between subregions Ω_C and Ω_F.

In the equations to follow, quantities denoted by a subscript C, F, B or G represent the portion which corresponds to Ω_C, Ω_F, the boundary atom layer B, and the ghost atom (interfacial) layer G, as labelled in Figure 2. The subscript d indicates that the partial derivatives are with respect to the FEM nodal displacements $\mathbf{d}$ and similarly for $\mathbf{u}$. The atomic mass matrix, $\mathbf{M}_A$, is a diagonal matrix containing the mass of each MD atom. The superposed dots and $\mathbf{I}$ have the standard meanings of time derivative and the identity matrix. The use of the superscript ext refers to external contributions such as applied loads.

For the derivation we must consider an equation of motion for the total displacement in the domain Ω of the following form:

$$\mathbf{M}_A \ddot{\mathbf{u}} = -\nabla_u U(\mathbf{u}) + \mathbf{f}^{ext} \tag{2}$$

The first step in the development of BSM is to decompose the total displacement $\mathbf{u}$ into its coarse ($\bar{\mathbf{u}}$) and fine ($\mathbf{u}'$) parts. In order to do this, we will first define the coarse part and take the fine part as the remainder of the total displacement. In order to define the coarse scale part of $\mathbf{u}$, we define a coarse scale basis $\mathbf{N}(\mathbf{X}_\alpha)$ of size $n_f \times n_c$, where the variables denote the number of MD atoms

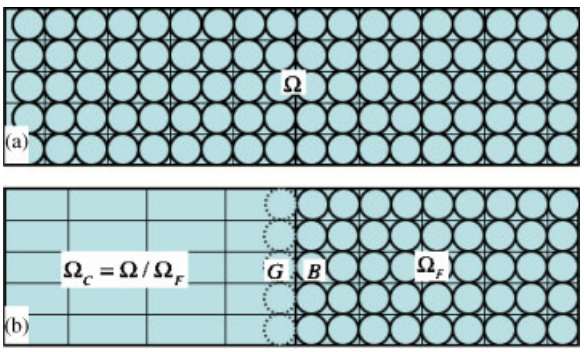

Figure 2. Schematic of domain to be considered for BSM formulation discussion: (a) initial domain, with coarse scale basis and atomistic information everywhere, used as a starting point and (b) final domain, for use in BSM. The atomistics have eliminated in subregion Ω_C *via* linear lattice mechanics principles.

DOI: 10.1002/nme

and FEM nodes, respectively. For the coupling case considered here, the entries in the matrix $\mathbf{N}$ are the FEM shape functions evaluated at the initial atomic positions, $\mathbf{X}_\alpha$. We may define the projection onto the coarse scale basis in many ways, but the most natural is to choose a projection that minimizes the difference between the total displacement and the coarse scale displacement. Therefore, we obtain the following:

$$\min[(\mathbf{u}-\mathbf{N}\mathbf{d})\mathbf{M}_\mathrm{A}(\mathbf{u}-\mathbf{N}\mathbf{d})] \rightarrow \mathbf{d}=\mathbf{M}^{-1}\mathbf{N}^\mathrm{T}\mathbf{M}_\mathrm{A}\mathbf{u}, \quad \mathbf{M}=\mathbf{N}^\mathrm{T}\mathbf{M}_\mathrm{A}\mathbf{N} \tag{3}$$

The coarse and fine scale parts of the displacement are then defined as

$$\text{Coarse: } \bar{\mathbf{u}}=\mathbf{N}\mathbf{d}=\mathbf{N}[\mathbf{M}^{-1}\mathbf{N}^\mathrm{T}\mathbf{M}_\mathrm{A}\mathbf{u}]=\mathbf{P}\mathbf{u} \tag{4}$$

$$\mathbf{P}=\mathbf{N}[\mathbf{M}^{-1}\mathbf{N}^\mathrm{T}\mathbf{M}_\mathrm{A}] \tag{5}$$

$$\text{Fine: } \mathbf{u}'=\mathbf{u}-\bar{\mathbf{u}}=(\mathbf{I}-\mathbf{P})\mathbf{u}=\mathbf{Q}\mathbf{u} \tag{6}$$

$$\mathbf{Q}=(\mathbf{I}-\mathbf{P}) \tag{7}$$

where $\mathbf{P}$ and $\mathbf{Q}$ are the coarse and fine scale projection operators, respectively. With these projections in hand, we can now obtain the equations of motion for the coarse and fine parts of the total displacement. To obtain these, we apply the projections to (2) and simplify to arrive at

$$\mathbf{M}\ddot{\mathbf{d}}=\mathbf{N}^\mathrm{T}[-\nabla_\mathrm{u}U(\mathbf{u})+\mathbf{f}^\mathrm{ext}]=-\nabla_\mathrm{d}U(\mathbf{N}\mathbf{d}+\mathbf{u}')+\mathbf{N}^\mathrm{T}\mathbf{f}^\mathrm{ext} \tag{8}$$

$$\mathbf{M}_\mathrm{A}\ddot{\mathbf{u}}'=\mathbf{Q}^\mathrm{T}[-\nabla_\mathrm{u}U(\mathbf{u})+\mathbf{f}^\mathrm{ext}] \tag{9}$$

Before we move on to restricting the fine scale system to a subregion of the total domain, some comments on the above system of equations are in order:

1. No empirical 'mixed Hamiltonian' or deformation gradient is used to define the equations of motion as in [6–8, 13]. The coarse and fine projections of the equations of motion lead to a natural set of coupled equations from the governing equations for the atomistic system. Thus, the resulting equations contain no *ad hoc* coupling terms.
2. If $\mathbf{N}$ goes to $\mathbf{I}$ then $\mathbf{P}$ goes to $\mathbf{I}$, then $\mathbf{d}\equiv\mathbf{u}$. This physically means that if the coarse scale points correspond to the atomic locations, then the coarse scale displacement is equivalent to the total displacement. Thus, if we were to refine the coarse scale mesh down to the atomic level, the coarse scale displacements would behave as the total displacement and the fine scale displacements would be zero.
3. The previous two points allow one to consider BSM to be a particle method, as the basis for the equations is the MD equation of motion (2). The separate equations for each scale are obtained through a straightforward projection of (2).

2.1. Elimination of fine scale degrees of freedom

Equations (8) and (9) completely define the coarse and fine scale motion across the entire domain Ω; however, we wish to restrict the fine scale calculations to a small subdomain of Ω in order to reduce the computational expense of the simulation. Further, since the fine scale information is available in Ω_F but not in Ω_C, we must couple the two regions such that the interface between

DOI: 10.1002/nme

the two allows waves to propagate naturally. Without appropriate interfacial conditions, one can observe spurious wave reflections as waves try to propagate out of Ω_F, as well as unphysical energy transfer across the interface [22, 37] between Ω_F and Ω_C. Thus, the final steps are to restrict the explicit solution of (9) to a subregion of Ω, and determine an appropriate interfacial condition.

Following the general idea proposed in the work of Adelman and co-workers [38–40], we seek an analytical solution for the fine scale motion at the interface between Ω_F and Ω_C which implicitly accounts for the dynamics of the eliminated fine scale degrees of freedom. As we do this, it is convenient if we are able to describe the motion of all of the unit cells in the domain by a single equation. One way to do this is to linearize the interactions between atoms (i.e. the internal force, $-\nabla_u U(\mathbf{u})$) and obtain an equation which describes the forces acting on any given atom in terms of a summation over the atom's neighbours. For the nearest neighbour hexagonal lattice used in this work (see Figure 3), we arrive at the following linearized fine scale equation of motion:

$$\ddot{\mathbf{u}}'_{n,m}(t) = \sum_{n'=n-2}^{n+2} \sum_{m'=m-1}^{m+1} \mathbf{M}_A^{-1} \mathbf{K}_{n-n',m-m'} \mathbf{u}'_{n,m}(t) + \mathbf{M}_A^{-1} \mathbf{f}^{\text{ext}}_{n,m}(t) \tag{10}$$

$$\mathbf{K}_{n-n',m-m'} = -\left. \frac{\partial^2 U}{\partial \mathbf{u}_{n',m'} \partial \mathbf{u}_{n,n}} \right|_{\mathbf{u}=0} \tag{11}$$

where $\mathbf{M}_A$, $\mathbf{K}_{n-n',m-m'}$, U and $\mathbf{f}^{\text{ext}}_{n,m}(t)$ denote the diagonal atomic mass matrix, lattice stiffness matrices, interatomic potential and the external force vector. The indices n, m are the atom indices in the unit cell. The lattice stiffness matrices are a generalization of linear spring stiffnesses to

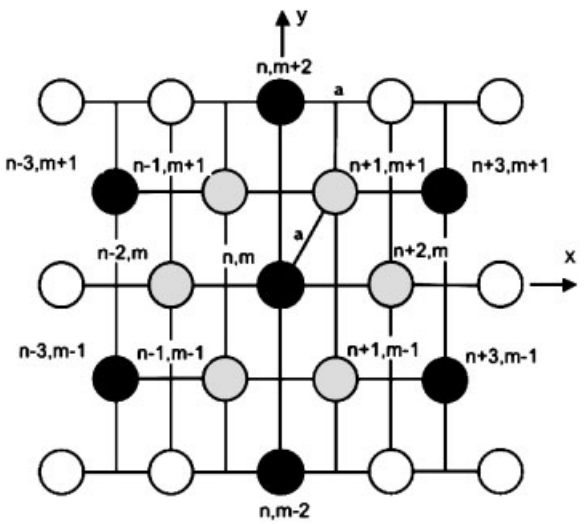

Figure 3. Schematic of hexagonal lattice, including atom indices. Light grey circles indicate the nearest neighbour atoms for atom n, m.

DOI: 10.1002/nme

multiple dimensions and are analogous to the FEM stiffness matrix [36]. Additionally, the lattice stiffness matrices are constant for a given lattice type and interatomic potential, and do not vary as the simulation progresses. The atom indices indicate the position of an atom within the unit cell basis. For the system illustrated in Figure 3, the centre atom n, m is the origin and the basis vectors are in the horizontal and vertical directions, with positive being towards the right and top, respectively.

In this work we choose the ghost atom layer (G in Figure 2(b)) to act as the interface. The ghost atoms are a layer of atoms adjacent to the boundary of the MD simulation and lie within Ω_C. These atoms are used to apply the interfacial condition to the 'real' atoms in Ω_F. Additionally, the ghost atoms ensure that the boundary atoms, B in Figure 2(b), as well as the other 'real' atoms are fully co-ordinated as though they were in the bulk. However, as their motion is not determined explicitly during the MD solution process, we must prescribe their fine scale fluctuations in some way. This prescription is precisely what the results of this section will provide. For the development shown here, we shall consider the ghost and boundary atom planes to be parallel to the x-axis, with the normal along the positive y-axis displayed in Figure 3.

The next step is to realize that the influence of the degrees of freedom to be eliminated on the remaining atoms can be described by an external force acting only on the interfacial atoms (in this case, the ghost atoms G in Figure 2(b)). Thus, the external force term in (10) becomes

$$\mathbf{f}^{\text{ext}}_{n,m}(t) = \delta_{m,G}\mathbf{f}^{\text{ext}}_{n,G}(t) \tag{12}$$

The basic idea of the interfacial condition is to obtain an analytical solution to (10), with the external force defined in (12), for the displacement of the ghost atoms in terms of the displacement of the boundary atoms (G and B in Figure 2(b), respectively). In order to do this, we make use of a Green's function approach to solve (10). We take the Laplace and discrete Fourier transform of (10), and solve for the corresponding displacement in mixed Fourier–Laplace space, $\hat{\mathbf{U}}(p, q, s)$,

$$\hat{\mathbf{U}}(p, q, s) = \hat{\mathbf{G}}(p, q, s)\mathbf{M}_A^{-1}\hat{\mathbf{F}}^{\text{ext}}_G(p, s) + \hat{\mathbf{R}}(p, q, s) \tag{13}$$

$$\hat{\mathbf{R}}(p, q, s) = \hat{\mathbf{G}}(p, q, s)[s\hat{\mathbf{u}}(p, q, 0) + s\hat{\dot{\mathbf{u}}}(p, q, 0)] \tag{14}$$

$$\hat{\mathbf{G}}(p, q, s) = (s^2\mathbf{I} - \hat{\mathbf{A}}(p, q))^{-1} \tag{15}$$

$$\hat{\mathbf{A}}(p, q) = \mathscr{F}_{n,m\to p,q}\{\mathbf{M}_A^{-1}\mathbf{K}_{n,m}\} \tag{16}$$

where the hatted notation refers to mixed Fourier–Laplace transformed quantities, (p, q) corresponds to the spatial indices (n, m), and s is the Laplace variable corresponding to the time t. The quantity denoted by $\hat{\mathbf{G}}(p, q, s)$ is the lattice Green's function, the building block for our solution. The term $\hat{\mathbf{R}}(p, q, s)$ corresponds to the initial conditions which come from the Laplace transform and will be explained further later in this section. The next step is to take an inverse discrete Fourier transform of (13) with respect to q (the index in the direction of m). This gives us an expression for any plane of atoms with a normal in the direction of m, in terms of the lattice Green's function (15) and the applied force in Fourier–Laplace space

$$\tilde{\mathbf{U}}_m(p, s) = \tilde{\mathbf{G}}_m(p, s)\mathbf{M}_A^{-1}\hat{\mathbf{F}}^{\text{ext}}_G(p, s) + \tilde{\mathbf{R}}_m(p, s) \tag{17}$$

DOI: 10.1002/nme

where the tilde denotes that a partial inverse Fourier transform has been applied. This results in the following two equations for the ghost plane (denoted by subscript G) and the boundary plane (denoted by subscript B):

$$\tilde{\mathbf{U}}_G(p,s) = \tilde{\mathbf{G}}_G(p,s)\mathbf{M}_{\mathrm{A}}^{-1}\hat{\mathbf{F}}_G^{\mathrm{ext}}(p,s) + \tilde{\mathbf{R}}_G(p,s) \tag{18}$$

$$\tilde{\mathbf{U}}_B(p,s) = \tilde{\mathbf{G}}_B(p,s)\mathbf{M}_{\mathrm{A}}^{-1}\hat{\mathbf{F}}_G^{\mathrm{ext}}(p,s) + \tilde{\mathbf{R}}_B(p,s) \tag{19}$$

Solving for $\hat{\mathbf{F}}_G^{\mathrm{ext}}$ in (19) and substituting the result into (18), we obtain an expression for the displacement of the ghost atoms in terms of the boundary atoms,

$$\tilde{\mathbf{U}}_G(p,s) = \tilde{\mathbf{Q}}(p,s)[\tilde{\mathbf{U}}_B(p,s) - \tilde{\mathbf{R}}_B(p,s)] + \tilde{\mathbf{R}}_G(p,s) \tag{20}$$

where

$$\tilde{\mathbf{Q}}(p,s) = \tilde{\mathbf{G}}_G(p,s)\tilde{\mathbf{G}}_B(p,s)^{-1} \tag{21}$$

In order to obtain the real space equation for the fine scale motion of the ghost atoms from (20), we need to take an inverse discrete Fourier transform with respect to p, and an inverse Laplace transform. The result, which takes into account the effects of the eliminated degrees of freedom, is as follows:

$$\mathbf{u}'_{n,G} = \sum_{n'=-N/2}^{N/2} \int_0^t \mathbf{\Theta}_{n-n'}(t-\tau)[\mathbf{u}'_{n',B}(\tau) - \mathbf{R}_{n',B}(\tau)]\,\mathrm{d}\tau + \mathbf{R}_G(t) \tag{22}$$

where $\mathbf{\Theta}(t)$ is the so-called time history kernel (THK), the inverse transform of (21). The THK is a set of matrices that relate the dynamics of adjacent atoms in the system and are the key to the interfacial condition, as they allow the interfacial atoms to behave as if they were part of a much larger system. The terms $\mathbf{R}_B(t)$ and $\mathbf{R}_G(t)$ are random displacement terms which stem from the initial conditions present in the Laplace transform of (10). These may be used to account for finite temperature effects as proposed in [41]. In this work, we take them to be zero, thus exclusively considering zero temperature dynamic problems.

To compute $\mathbf{\Theta}(t)$, we must take an inverse Fourier transform and an inverse Laplace transform of (21). The inverse discrete Fourier transform is straightforward, and may be computed readily. However, for the case considered here the inverse Laplace transform cannot to the authors' knowledge be determined analytically, thus a numerical algorithm is required. Previous work by Liu and co-workers [22–25] made use of the Weeks algorithm [42], which uses Laguerre polynomials to invert the transform.

In this work, we have moved to a new inverse transform technique based on the work of Crump [43], which instead uses a Fourier series approach. The advantage of the new approach lies primarily in the fact that it does not require special functions to be defined, only the ability to use complex numbers, exponentials and sinusoidal functions. This makes the algorithm easier to implement in a program such as Matlab, or in high level programming languages such as C++ or Fortran. Additionally, the technique has also been seen to allow for the use of fewer terms, resulting in a reduced computational expense (see Figure 4, which illustrates this for a simple 1D case where an analytic solution exists). The resulting inverse formula for the present case is as

DOI: 10.1002/nme

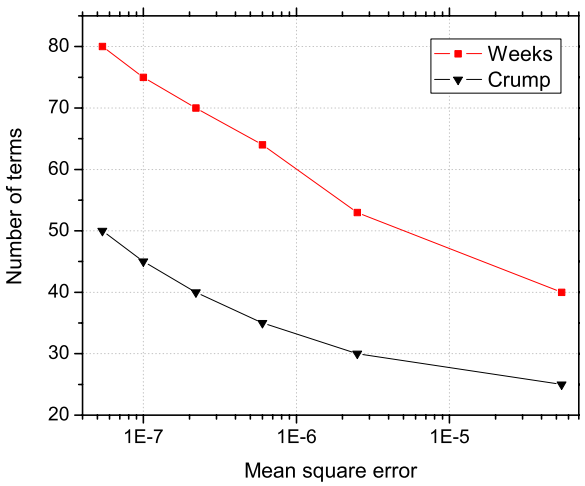

Figure 4. Mean-squared error between the Weeks and Crump numerical inverse Laplace transform schemes and analytical solution for a model 1D nearest neighbour harmonic lattice THK. Note that Crump's method requires fewer terms for similar accuracy.

follows: first, take the Fourier inverse of (21),

$$\mathbf{Q}_n(s) = \frac{1}{N} \sum_{p=1-N/2}^{N/2} \tilde{\mathbf{Q}}(p, s)\, \mathrm{e}^{4\mathrm{i}\pi pn/N} \tag{23}$$

then compute the Laplace inverse using the method of Crump [43],

$$\mathbf{\Theta}_n(t) = -2\, \frac{\mathrm{e}^{-at}}{t_{\max}} \sum_{\xi=1}^{N_{\text{modes}}} \mathrm{Im}\{\mathbf{Q}_n(\xi)\} \sin\left(\frac{\xi \pi t}{t_{\max}}\right) \tag{24}$$

where N denotes the number of atoms in each direction in the numerical inverse domain, a and N_{modes} are the two inverse parameters, where a must be a small positive number ($0<a<1$), and N_{modes} is the number of sine modes to use in the inverse. Finally, $t_{\max}$ is the maximum time for the numerical inverse, typically taken to be slightly longer than the length of time for which the convolution is to be computed in (22). We take $t_{\max}$ slightly longer to ensure a good solution for the Laplace inverse over the entire convolution period.

Before continuing onto the next section, several notes are in order:

1. Equation (10) is required to be valid in the vicinity of the THK boundary. This is due to the fact that we only make use of the linearization in the fine scale equation of motion at the ghost atom layer, the boundary atom layer, and in the eliminated region. Thus, inside Ω_{F} away from the boundary, we may have non-linear behaviour (both geometric and material). This is the case in the simulations to be discussed in this paper.
2. As the linearity requirement was only applied to $\mathbf{u}'$ in Ω_{C}, which has in turn been eliminated by (22), we have not placed any linearity constraints on $\bar{\mathbf{u}}_{\mathrm{C}}$. This allows the use of non-linear material models and geometric non-linearities in Ω_{C} [24, 25].

DOI: 10.1002/nme

3. Equation (15) describes a simplified lattice Green's function compared to that derived in [23]. This simplification was reported in [23] to induce numerical errors at the interface, however, it is less expensive to compute. An alternative definition of (16) was proposed in [23] utilizing the fine scale projection $\mathbf{Q}$ and the full matrix $\mathbf{K}$ for the system,

$$\hat{\mathbf{A}}^*(p,q) = \mathscr{F}_{n,m\to p,q}\{\mathbf{M}_{\mathrm{A}}^{-1}\mathbf{Q}^{\mathrm{T}}\mathbf{K}\} \tag{25}$$

4. In general, the calculation of (22) can be expensive over long times and for large interfaces. Thus, as discussed in [27, 36] we truncate the evaluation of the convolution and summations to some critical region:

$$\mathbf{u}'_{n,G} = \sum_{n'=n-N\mathrm{crit}}^{n+N\mathrm{crit}} \int_0^{t_{\mathrm{crit}}} \mathbf{\Theta}_{n-n'}(t-\tau)[\mathbf{u}'_{n',B}(\tau) - \mathbf{R}_{n',B}(\tau)]\,\mathrm{d}\tau + \mathbf{R}_G(t) \tag{26}$$

2.2. *Course/fine coupling*

Using the condition given by (26), we no longer have fine scale information in Ω_{C}. Thus, we need to adjust (8) to reflect this fact. The resulting coarse scale equation is as follows:

$$\mathbf{M}\ddot{\mathbf{d}} = \mathbf{N}^{\mathrm{T}}[-\nabla_{\mathrm{u}}U(\tilde{\mathbf{u}})] + \mathbf{N}^{\mathrm{T}}\mathbf{f}^{\mathrm{ext}} \tag{27}$$

$$\tilde{\mathbf{u}} = \begin{bmatrix} \mathbf{u}_{\mathrm{F}} \\ \\ \bar{\mathbf{u}}_{\mathrm{C}} \end{bmatrix} \tag{28}$$

where $\bar{\mathbf{u}}_{\mathrm{C}}$ is the course scale part of the displacement in Ω_{C}, as given by the coarse scale projection in (4). The term $\mathbf{N}_{\mathrm{F}}^{\mathrm{T}}[-\nabla_{\mathrm{u}}U(\mathbf{u}_{\mathrm{F}})]$ corresponds to a straightforward projection of the interatomic forces to obtain the FEM internal forces in Ω_{F}. Meanwhile, for the internal force in Ω_{C}, i.e. $\mathbf{N}_{\mathrm{C}}^{\mathrm{T}}[-\nabla_{\mathrm{u}}U(\bar{\mathbf{u}}_{\mathrm{C}})]$ we can make use of any constitutive relation which is consistent with the underlying atomistics, such as the Cauchy–Born model [5, 6, 44] or the virtual atom cluster (VAC) method [45].

As mentioned in the formulation section, we choose to make use of an MD system in Ω_{F} whose solution satisfies (2), with boundary conditions for the fine scale motion of the ghost atoms provided by (26). However, the MD solution is the total displacement, $\mathbf{u}_{\mathrm{F}}$, thus it is convenient to also write (26) in terms of the total displacement. We can do this by recalling (1), which when combined with (26), allows us to easily obtain a non-reflecting boundary condition to be applied to the MD simulation,

$$\mathbf{u}_{n,G} = \bar{\mathbf{u}}_{n,G} + \sum_{n'=n-N\mathrm{crit}}^{n+N\mathrm{crit}} \int_0^{t_{\mathrm{crit}}} \mathbf{\Theta}_{n-n'}(t-\tau)[\mathbf{u}_{n',B}(\tau) - \bar{\mathbf{u}}_{n',B}(\tau)]\,\mathrm{d}\tau \tag{29}$$

where $\bar{\mathbf{u}}_G$ and $\bar{\mathbf{u}}_B$ are obtained by interpolating the FEM displacements to the ghost and boundary atoms based on their initial positions as follows:

$$\bar{\mathbf{u}}_G = \mathbf{N}(\mathbf{X}_G)\mathbf{d} \tag{30}$$

$$\bar{\mathbf{u}}_B = \mathbf{N}(\mathbf{X}_B)\mathbf{d} \tag{31}$$

DOI: 10.1002/nme

2.3. Summary of BSM

To summarize, the coarse scale equation (27) represents a standard FEM system which obtains its constitutive model differently from two distinct material regions. The first material region is in Ω_F (see Figure 2(b)), where the nodal internal forces are determined by a projection of the interatomic forces, i.e. $\mathbf{N}_F^T[-\nabla_u U(\mathbf{u}_F)]$. The second is the continuum-only region, Ω_C (see Figure 2(b)) where the internal force, $\mathbf{N}_C^T[-\nabla_u U(\bar{\mathbf{u}}_C)]$, is determined by a constitutive law based on the underlying atomic structure. In the numerical examples to be shown in this work, we use the Cauchy–Born material model [5, 6, 44]; however, a model such as the VAC [45] may also be used and may be preferable in general due to its projection-based nature. The MD equation is simply the standard MD equation of motion (2). The ghost atom equation, (29), acts as a boundary condition to the MD simulation and allows short wavelengths generated within the MD region that cannot be resolved by the FEM to dissipate naturally. The coupling provided by the $\mathbf{N}_F^T[-\nabla_u U(\mathbf{u}_F)]$ term in the FEM equations for the Ω_F material region provides the ability for coarse scale waves to propagate from Ω_C to Ω_F and *vice versa* (Table I).

Due to the different length scales present in the MD and FEM regions, we make use of a staggered time integration scheme to integrate the MD and FE equations of motion; details can be found in Liu and co-workers [22–25]. Specifically, we utilize a central difference (or velocity Verlet) scheme for both the FEM and MD. In the simulations presented here we utilized a 10:1 MD:FEM timestep ratio. It is important to note that we made use of the central difference scheme for ease; however, there are no points in the BSM formulation which would restrict the use of higher-order time integration schemes. The full algorithm as implemented in the Sandia National Laboratories open source simulation code, Tahoe [46] as well as the THK code used are given in Appendix A.

Table I. Summary of BSM equations.

Remarks	Equations
Displacement decomposition	$\mathbf{u} = \bar{\mathbf{u}} + \mathbf{u}'$
Course scale projection	$\mathbf{P} = \mathbf{N}\mathbf{M}^{-1}\mathbf{N}^T\mathbf{M}_A$ $\bar{\mathbf{u}} = \mathbf{P}\mathbf{d}$
Fine scale projection	$\mathbf{Q} = \mathbf{I} - \mathbf{P}$ $\mathbf{u}' = \mathbf{Q}\mathbf{u}$
Course scale (FEM in Ω)	$\mathbf{M}\ddot{\mathbf{d}} = \mathbf{N}^T[-\nabla_u U(\tilde{\mathbf{u}})] + \mathbf{N}^T\mathbf{f}^{ext}$ $\tilde{\mathbf{u}} = \begin{bmatrix} \mathbf{u}_F \\ \bar{\mathbf{u}}_C \end{bmatrix}$
Fine scale (MD in Ω_F)	$\mathbf{M}_{A,F}\ddot{\mathbf{u}}_F = -\nabla_u U(\mathbf{u}_F) + \mathbf{f}_F^{ext}$
Fine scale interface condition	$\mathbf{u}_{n,G} = \bar{\mathbf{u}}_{n,G} + \sum_{n'=n-N\text{crit}}^{n+N\text{crit}} \int_0^{t_{\text{crit}}} \boldsymbol{\Theta}_{n-n'}(t-\tau)[\mathbf{u}_{n',B}(\tau) - \bar{\mathbf{u}}_{n',B}(\tau)]\,\mathrm{d}\tau$ $\boldsymbol{\Theta}_n(t) = \mathscr{L}^{-1}\mathscr{F}_{p\to n}^{-1}\{\tilde{\mathbf{G}}_G(p,s)\tilde{\mathbf{G}}_B(p,s)^{-1}\}$ $\bar{\mathbf{u}}_G = \mathbf{N}(\mathbf{X}_G)\mathbf{d}, \quad \bar{\mathbf{u}}_B = \mathbf{N}(\mathbf{X}_B)\mathbf{d}$

DOI: 10.1002/nme

3. APPLICATION OF BSM TO INTERSONIC CRACKS

In this section we will present two sets of data: one set will be the benchmark MD solution, the other will be the BSM result. Here, the MD solution is obtained using the same integration method and parameters as the MD part of the BSM. All of the simulations discussed in this paper were performed with the Sandia National Laboratories open source simulation code Tahoe [46]. We seek to further test the abilities of BSM, particularly the wave dissipation abilities and the applicability of BSM to shear dominant fracture scenarios. Note that all times and units used in the remainder of the text are normalized to be consistent with the potential parameters used thus unit names will not be given. All simulations were performed using these normalized parameters.

The system under consideration is shown in Figure 5. The body is modelled as a perfectly elastic 2D hexagonal lattice with nearest neighbour interactions that are described by the following harmonic potential:

$$U_{\text{harmonic}} = \tfrac{1}{2}\, k(r_{ij} - r_0)^2 \tag{32}$$

where k is the stiffness constant, r_0 is the equilibrium separation distance while r_{ij} is the centre to centre distance between atoms i and j. Harmonic bodies have an infinite fracture strength as there is no bond softening or breaking accounted for by the potential, i.e. no transition from positive to negative concavity. Thus, some modifications to the system are required if bond breaking

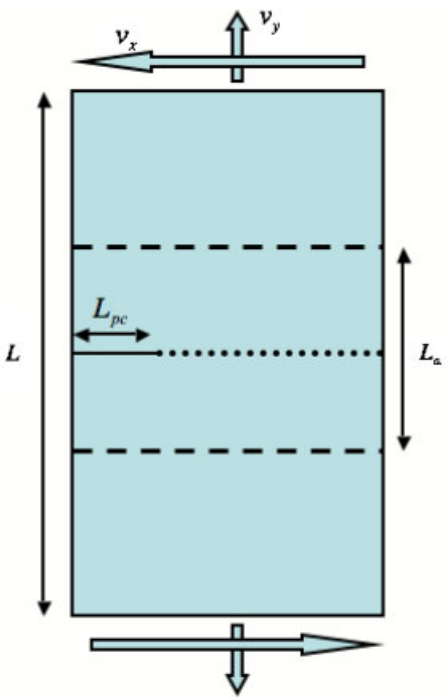

Figure 5. Schematic of 2D edge crack system. BSM simulations were performed at the following ratios: $(L_a/L \approx \frac{1}{6})$; $(L_a/L \approx \frac{1}{3})$ and $(L_a/L \approx \frac{1}{2})$.

DOI: 10.1002/nme

and fracture processes are to be considered. In order to allow fracture to occur as well as to constrain the crack so that it does not branch and reduce the velocity of the main crack tip, we introduce a 'weak' plane of atoms with a finite fracture toughness. This 'weak' plane is defined by two rows of atoms along the centreline (dotted lines in Figure 5) with nearest neighbour interactions described by the following Lennard-Jones potential:

$$U_{\mathrm{LJ}} = 4\varepsilon\left[\left(\frac{\sigma}{r_{ij}}\right)^{12} - \left(\frac{\sigma}{r_{ij}}\right)^{6}\right] \tag{33}$$

where ε and σ are the scaling parameter for the 'depth' of the potential well and the potential shape parameter, respectively.

We also prescribe an edge pre-crack in order to facilitate crack initiation. The pre-crack is defined as two partial rows of non-interacting atoms at the left side of the weak plane (solid line in Figure 5). The Lennard-Jones potential contains bond softening, as the potential transitions from positive concavity to negative past a certain critical bond length (i.e. the inflection point where $\mathrm{d}^2U_{\mathrm{LJ}}/\mathrm{d}r_{ij}^2 = 0$). During the simulation, the only neighbouring atoms which do not interact are those in the precrack which only interact with neighbours on the same side of the centreline.

The parameters for the Lennard-Jones potential were $\sigma = \varepsilon = \text{mass} = 1.0$ in scaled units (sometimes referred to as Lennard-Jonesium). The harmonic potential used parameters consistent with the Lennard-Jones potential linearized about equilibrium, i.e. $\text{mass} = 1$, $k = \frac{72}{2}^{1/3}$ and both potentials used an equilibrium separation of $r_0 = 2^{1/6}$ [35]. For the coarse scale model in the BSM simulations, we utilized a Cauchy–Born material model in the continuum-only region based on the parameters for the harmonic potential, while the internal forces at the FEM nodes in the overlap region were obtained based on the projection of the interatomic forces as mentioned in the BSM summary.

For the simulations, we created an MD model with a total height L of 600 atoms, and an $x{:}y$ aspect ratio of 1:2. The precrack size L_{pc} was fixed at 100 atoms (50 in upper row, 50 in lower). For the BSM models, we maintained the same outer dimensions for the FEM system as the full MD system; however, in order to demonstrate the atomistic region size effects on the results we varied the height of the atomistic section, L_{a} to 103, 203 and 303 atoms. These sizes correspond to $(L_{\mathrm{a}}/L \approx \frac{1}{6})$, $(L_{\mathrm{a}}/L \approx \frac{1}{3})$ and $(L_{\mathrm{a}}/L \approx \frac{1}{2})$, respectively. The numbers following the letters BSM in the figures to follow denote the number of rows of atoms in the fine scale region. For the BSM, the FEM mesh consisted of 30×60 bilinear quadrilateral elements, with roughly 102 atoms per element. The system was loaded *via* velocity boundary conditions on the top and bottom surfaces, with a horizontal strain rate of $\dot{\varepsilon}_x = 0.00086$, and a vertical strain rate of $\dot{\varepsilon}_y = 0.00017$ which correspond to the applied velocities, $v_x = 0.25$ and $v_y = 0.05$ applied to the upper and lower faces. This loading condition represents a situation in which we may observe a shear-dominant mixed-mode crack, rather than pure mode-II crack development; this allows for a clearer definition of the crack opening.

3.1. Results

We first ran the full MD model in order to establish a benchmark to compare with the BSM models. For all of the simulations discussed in this paper, the MD is taken as the analytic solution to which the BSM simulation results will be compared.

DOI: 10.1002/nme

By examining the crack-tip position as a function of time (Figure 6), we can see four distinct regions. The first region (**I**) is simply zero displacement, as it is prior to crack initiation. This region leads into the first phase of crack propagation (**II**), in which the crack propagates at a sub-Rayleigh velocity. The slope of the MD plot in this region is roughly 2.74 (compared to the Rayleigh velocity, $c_R \approx 4.83$ [34, 35]) and the BSM slopes differ from the MD by a maximum of roughly 2.6%. An abrupt transition is visible at around time 80 (**III**), when the crack enters the intersonic regime (faster than the shear wave speed, $c_s = 5.2$, but slower than the longitudinal wave speed, $c_l = 9$ [34, 35]). In this third region, the MD crack-tip velocity is roughly 7.4 (compared to 8.97 from [34, 35]) and the BSM differ from the MD by a maximum of roughly 12%. Note that the biggest differences between crack-tip positions begin to appear late in this phase of propagation. Finally, at roughly time = 100 (**IV**) the body fractures fully, and the results with the exception of 103 agree with this time, while 203 differs by roughly 3%. These findings are in general agreement as to the trends demonstrated by the work of Gao and co-workers [34, 35]. However, the magnitudes of the crack-tip velocities are reduced as compared to their simulations, due to the smaller domain size considered in this work.

In order to better understand what is happening in the region near the crack plane, we examine the total energy in the system in Figure 7. The plot is for the centre 99 rows of atoms with the crack plane in the middle ($L_a/L \approx \frac{1}{6}$), as this allows us to compare the results for all of the systems on equal ground because we sample the energy from the same spatial region in each case. From Figure 7, we see that in region **I**, prior to crack opening, we have very good agreement between the MD and BSM systems. However, after the crack begins to propagate, the BSM systems have a slight difference in energy transmission at the onset of fracture (region **II**), but the rate of energy transmission remains roughly the same. Late in region **II**, it becomes clear that the BSM solution is dependent on the number or rows of atoms in the fine scale region. The 103 row simulation

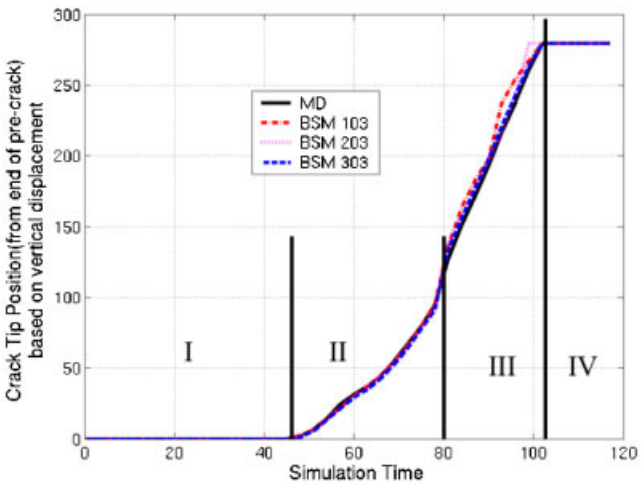

Figure 6. Crack-tip position during the simulation. Displacement determined by vertical separation of crack path layers. Note four distinct regions—no crack (**I**), initial (sub-Rayleigh) crack (**II**), accelerated (intersonic) crack (**III**) and complete fracture (**IV**). Simulation time is in units consistent with the potential as noted in the text.

DOI: 10.1002/nme

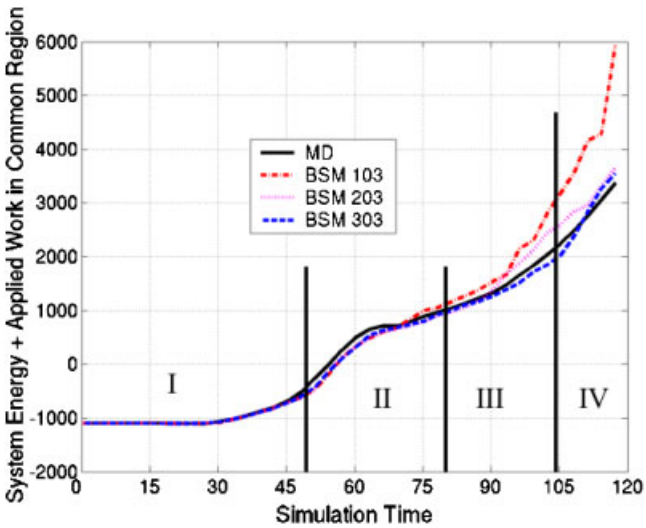

Figure 7. Total energy plus work in vicinity of crack plane. The four regions discussed in the crack-tip plot are labelled here by Roman numerals. Simulation time is in units consistent with the potential as noted in the text.

clearly is not realistic from an energetic standpoint, as the behaviour appears divergent, similar to the observations of Park and co-workers [24] for small system sizes under tensile loading. The energy plots for the 203 and 303 cases are more akin to the MD response, though each begins to differ as the point of final fracture approaches. The final energy is similar, indicating that the energy dissipation at the interface is sufficient to not affect the physics of the problem.

To further explore the deviation of the BSM results as the system approaches complete fracture, we may examine Figure 8. This figure illustrates the size of the Mach cone in the MD simulation at time 96, just prior to full fracture. The labelled lines denote the boundaries of Ω_F for each of the BSM cases at this same time. We hypothesize that the system energy in Figure 7 for the BSM 103 and 203 systems grows due to the dimensions of the Mach cone, which eventually exceeds Ω_F for both cases. Note that the 203 case loses accuracy later, at time 90 in Figure 7 as compared to the 103 case which diverges at time 75 in the same figure; this occurs due to the increased size of the 203 region which accommodates a longer period of Mach cone growth. The results for the 303 case are relatively unaffected for the simulation duration, as full fracture occurs prior to the Mach cone passing over the boundary of Ω_F. As this work is ongoing, a detailed mathematical analysis of this phenomenon is left for future work.

In the simulations performed, we observed the formation of a daughter crack as reported in [34, 35] as well as the resulting crack-tip acceleration into the intersonic regime and the formation of a Mach cone, though in the 103 case it is not as clearly defined due to reflections at the interface. Figure 9 shows two images of the Mach cone formation, one with the partially formed cone (a) and the second with the propagating cone (b). We also observe that as the crack propagates, a small opening appears and propagates away from the main crack, i.e. the daughter crack (Figure 10(a) and (b)). The daughter crack leaves a zone of material in its wake in which the upper plane of crack path atoms is almost in line with the lower crackpath atoms (Figure 10(c)). As this perturbed

DOI: 10.1002/nme

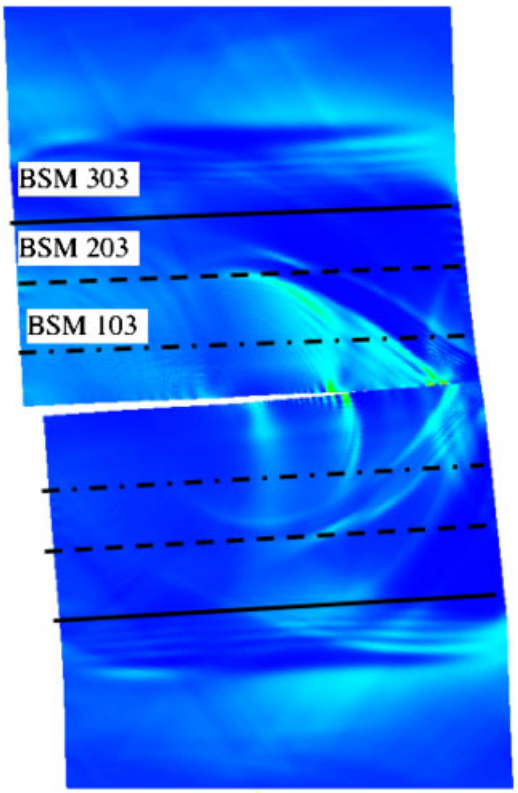

Figure 8. Illustration of Mach cone in MD simulation at time = 96, just prior to full fracture. The labelled lines illustrate the boundaries of Ω_F for the different BSM cases. Note that for the BSM 103 and 203 cases, the Mach cone extends beyond the boundary of Ω_F. Full fracture occurs prior to the Mach cone affecting the BSM 303 case. Colouration is kinetic energy.

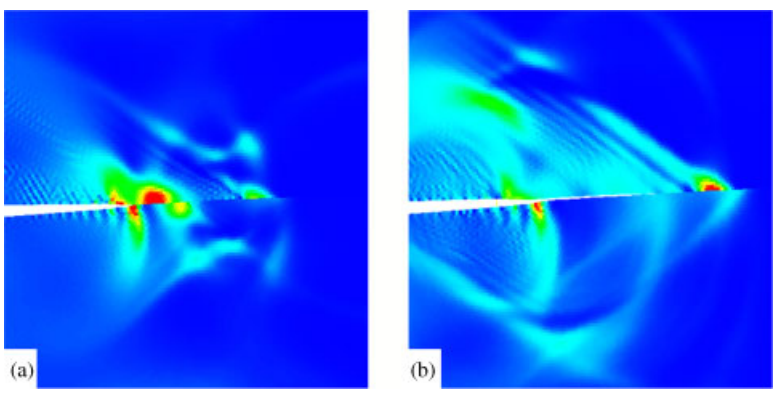

Figure 9. Detail of BSM 303 Mach cone formation: (a) daughter crack has begun to accelerate, Mach cone partially formed at time 80 and (b) time 85, Mach cone has clearly formed. Colouration is kinetic energy.

DOI: 10.1002/nme

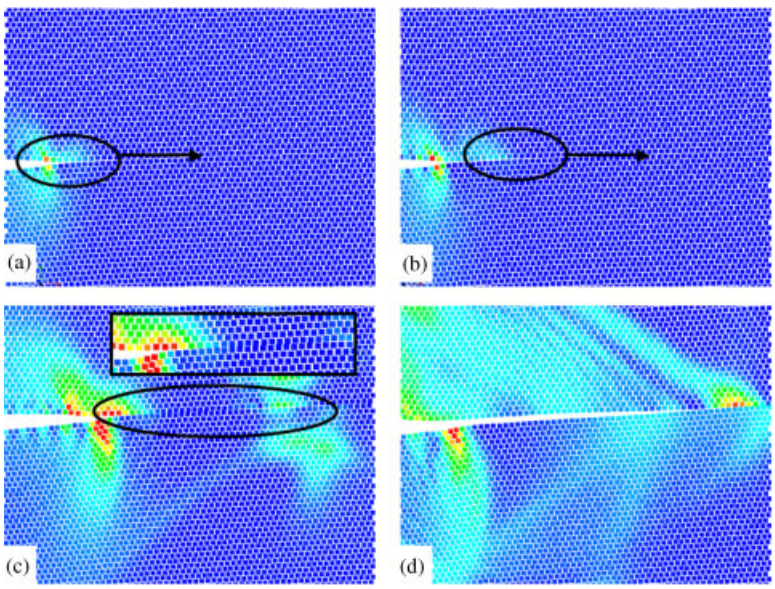

Figure 10. Detail of BSM 303 crack tip: (a) daughter crack forms directly ahead of main crack; (b) daughter crack accelerates away from main crack; (c) daughter crack leaves perturbed region in wake (see inset); and (d) due to weaker perturbed region in (c), main crack propagates more quickly, joins with daughter crack. Colouration is kinetic energy.

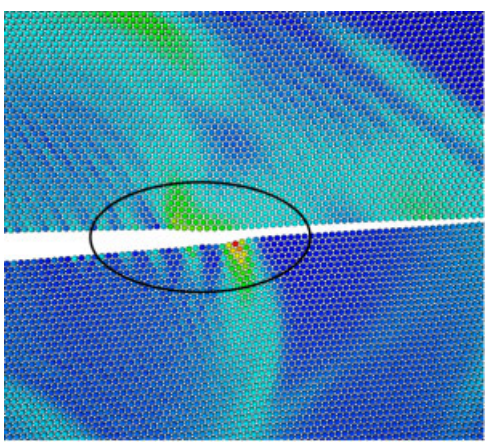

Figure 11. Detail of BSM 303 crack tip after daughter crack formation. Note the distinct asymmetry at the main crack tip (in the circled region). Colouration is kinetic energy.

lattice has a reduced energy barrier to separation, the crack may propagate more quickly and join with the daughter crack. These findings are in agreement with those presented by Abraham and Gao [34] and Gao *et al*. [35], though they did not discuss in detail the mechanism which resulted in the merging of the daughter and main crack. Further, we also note asymmetry of the crack tip as reported in [34, 35] as demonstrated in Figure 11.

DOI: 10.1002/nme

The energy plot presented earlier (Figure 7) indicates that the energy propagation out of the overlap region is similar to that of the pure MD calculation during the time the Mach cone is present (region III in Figure 7) but loses accuracy just prior to full fracture. This leads to the conclusion that the Mach cone reacts in the BSM as it does in the pure MD calculation prior to full fracture. By inspection of Figure 12 we see that this is indeed the case, as the coarse scale part propagates and we see no fine scale reflections, with the exception of the BSM 103 case, as seen in Figure 13.

It is apparent that the comparisons between the MD benchmark simulation and the BSM simulations are reasonable, indicating that the BSM is able to perform as well as an equivalent MD model for this scenario. Further, due to the projection used in the BSM for the FEM internal forces in the overlap region, we can capture the physics of fracture without resorting to specialized elements or mesh refinement as in standard FEM or quasicontinuum methods [5]. Figure 14 shows the distortion of the FEM mesh in the BSM simulations due to the presence of the crack in the MD region. Note that we need not refine the mesh, destroy or create elements, nor use special fracture elements. This property is one of the unique strengths of BSM, and is a direct result of the projection of the interatomic forces in (27) used to obtain the FEM constitutive relation in Ω_F. This projection avoids the computation of the deformation gradient or Jacobian for the finite

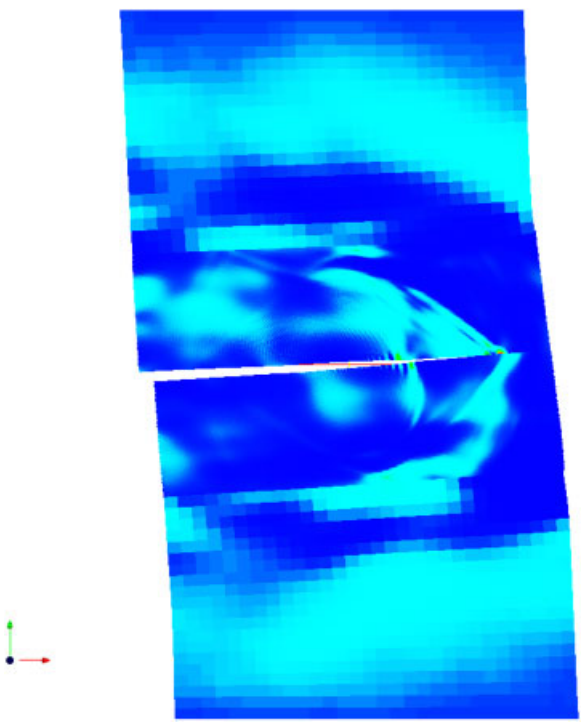

Figure 12. Illustration of wave propagation for BSM 203 case. Centre region with high resolution contains MD, lower resolution region denotes FEM only region. Note that the waves propagate naturally within the overlap region, however, at the THK interface, the fine scale part is dissipated and the coarse scale propagates.

DOI: 10.1002/nme

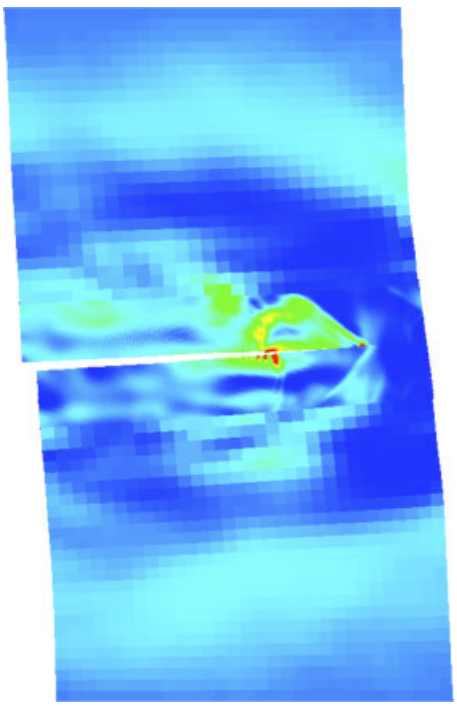

Figure 13. Illustration of wave reflection/propagation for BSM 103 case. Centre region with high resolution contains MD, lower resolution region denotes FEM only region. Note that the waves tend to remain in the overlap region, with incomplete damping and propagation compared to the 203 and 303 cases.

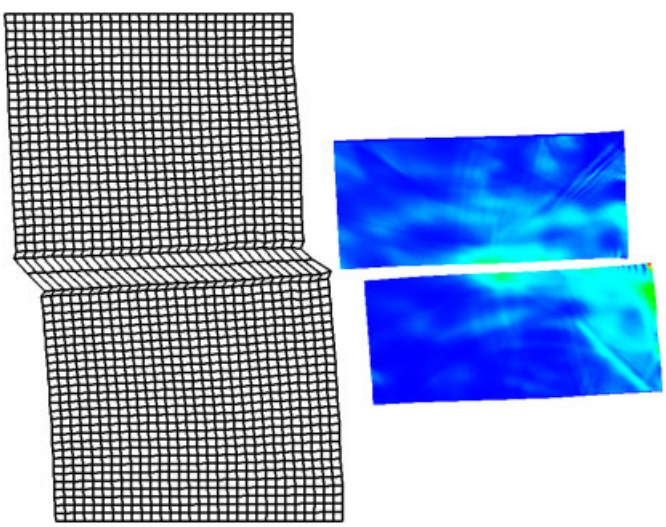

Figure 14. FEM mesh and MD region for BSM 303 simulation after complete fracture. The MD region has been moved to right so that it does not overlap the FEM region, for clarity.

DOI: 10.1002/nme

elements in Ω_F, thus allowing mesh distortions which would not be possible in a standard FEM simulation.

4. CONCLUSIONS

We have performed MD and BSM simulations of intersonic crack propagation along a weak plane in an elastic solid with a newly adopted technique for finding the damping kernel functions. By comparing the results of the BSM simulations for differing overlap region sizes to a benchmark MD solution, we have found that the simulations all show favourable agreement over time in system energy and crack-tip position/crack velocities. While agreement between BSM and MD simulations was shown to improve by increasing the size of the fine scale region in the BSM, accurate results using the BSM were obtained with fine scale system sizes that are considerably smaller than the size of the full MD system.

We have also demonstrated that the BSM interfacial condition can dissipate the strong localized waves and Mach cones generated by the crack tip, as the BSM and MD system energies were shown to match well during the later stages of the crack propagation. Additionally, we have observed the nucleation and acceleration of a daughter crack away from the main crack, in agreement with previous work of Abraham and co-workers [34, 35]. Further, we have observed the mechanism by which the main crack is able to join with the daughter crack, i.e. the daughter crack first develops ahead of the main crack tip, and accelerates away leaving a trail of weakened material in its wake. This trail allows the main crack to propagate faster and eventually join with the daughter crack. Finally, we have explicitly provided in the Appendices the details of our BSM implementation and a code for determining the THKs used in this work.

APPENDIX A: BSM ALGORITHM AS IMPLEMENTED IN TAHOE

Implementation by Farrell, Klein based on Park, Klein

1. Initial conditions given, applied.
   (a) Set up ghost and boundary atom arrays.
   (b) Determine THK table for required time period.
   Represented in $\mathbf{\Theta}_n(t) = -(2/t_{\max})\mathrm{e}^{-at} \sum_{j=1}^{N_{\text{modes}}} \mathrm{Im}\{\mathbf{Q}_n(j)\} \sin(j\pi t/t_{\max})$ form (from Crump).
   (c) Set up interpolation matrix $\mathbf{N}$.
   (d) Initialize MD, then project onto FEM in overlap region and initialize continuum only part of FEM.
   $\bar{\mathbf{u}}_G$ and $\bar{\mathbf{u}}_B$ determined from initial conditions.
   (e) Store ghost, boundary displacement history.
2. For each FEM timestep
   (a) For each of the MD subcycle timesteps
      i. Update $\bar{\mathbf{u}}_G$ and $\bar{\mathbf{u}}_B$ to current MD time using time integration scheme (central difference method).

DOI: 10.1002/nme

ii. Update $\mathbf{u}_G$ using THK convolution, $\bar{\mathbf{u}}_G$ and $\bar{\mathbf{u}}_B$

A. Determine new $\mathbf{u}'_G$ from
$\mathbf{u}'_{n,G} = \sum_{n'=n-N\text{crit}}^{n+N\text{crit}} \int_0^{t_\text{crit}} \mathbf{\Theta}_{n-n'}(t-\tau)[\mathbf{u}_{n',B} - \bar{\mathbf{u}}_{n',B}]\,\mathrm{d}\tau$
B. Obtain $\mathbf{u}_G$ from $\mathbf{u}_G = \bar{\mathbf{u}}_G + \mathbf{u}'_G$.
C. Apply $\mathbf{u}_G$ as BC to MD region, update any other BCs on MD.

iii. Solve MD equations i.e. $\mathbf{M}_{A,D}\ddot{\mathbf{u}}_\text{F} = -\nabla_\text{u} U(\mathbf{u}_\text{F}) + \mathbf{f}_D^\text{ext}$.
iv. Output data (if specified) and continue.

(b) Calculate internal force for FEM

i. In overlap region, $\mathbf{f}_D^\text{int} = \mathbf{N}^\text{T}[-\nabla_\text{u} U(\mathbf{u}_\text{F})]$, i.e. project MD internal forces between real atoms (ghost atom bonds not included).
ii. In FEM only region, $\mathbf{f}_\text{C}^\text{int} = \mathbf{N}^\text{T}[-\nabla_\text{u} U(\mathbf{u}_\text{C})] = \mathbf{N}^\text{T}[-\nabla_\text{u} U(\bar{\mathbf{u}}_\text{C})]$ i.e. $\mathbf{u}'_\text{C} \equiv 0[-\nabla_\text{u} U(\bar{\mathbf{u}}_\text{C})]$ determined by CB rule.

(c) Solve FEM equations in entire domain i.e. $\mathbf{M}\ddot{\mathbf{d}} = \mathbf{f}^\text{int} + \mathbf{f}^\text{ext}$.
(d) Interpolate FEM displacements, velocities, accelerations to ghost and boundary atoms, i.e. determine new $\bar{\mathbf{u}}_G$ and $\bar{\mathbf{u}}_B$.
(e) Output data (if specified) and continue.

APPENDIX B: MATLAB TIME HISTORY KERNEL CODE

The code used to determine the THK for the nearest neighbour hexagonal lattice considered here is available as a Matlab *m*-file from [47] called THKcode.m.

The code is set up to determine the THK for a $k = m = 1$ harmonic system, but the result can be scaled to fit any system, so long as the frequency $\omega = \sqrt{k/m}$ for the system linearized about equilibrium is known. The inputs to the code are defined in the comments, but it should be noted that the matrix inverse of the Laplace–Fourier image of the lattice Green's function (15) has been pre-computed and hard coded to save time and memory. The output is a series of matrices which are the coefficients A_ξ in a modified sine series for the top and bottom planes in the system used here, based upon (24),

$$\mathbf{\Theta}_n(t) = \omega \mathrm{e}^{-a\omega t} \sum_{\xi=1}^{N_\text{modes}} A_\xi \sin\left(\frac{\xi \pi \omega t}{t_\text{max}}\right) \tag{B1}$$

$$A_\xi = \frac{-2}{t_\text{max}} \operatorname{Im}\{\mathbf{Q}_n(\xi)\} \tag{B2}$$

ACKNOWLEDGEMENTS

The authors would like to acknowledge the support of the NSF, the NSF IGERT Program as well as the NSF-Navy Civilian Service Fellowship Program and the Army Research Office. We would also like to thank Dr Patrick Klein, Dr Eduard Karpov and Prof. Shaoqiang Tang for their input during this work.

DOI: 10.1002/nme

REFERENCES

1. Hughes TJR. *The Finite Element Method*: *Linear Static and Dynamic Finite Element Analysis* (1st edn). Prentice-Hall: Englewood Cliffs, NJ, 1987.
2. Belytschko T, Liu WK, Moran B. *Nonlinear Finite Elements for Continua and Structures* (1st edn). Wiley: Chichester, 2000.
3. Haile JM. *Molecular Dynamics Simulations* (1st edn). Wiley: Chichester, 1992.
4. Allen MP, Tildesley DJ. *Computer Simulation of Liquids* (1st edn). Oxford University Press: Oxford, 1987.
5. Tadmor EB, Phillips R, Ortiz M. Quasicontinuum analysis of defects in solids. *Philosophical Magazine A* 1996; **73**:1529–1563.
6. Miller R, Tadmor EB. The quasicontinuum method: overview, applications and current directions. *Journal of Computer-Aided Materials Design* 2003; **9**:203–239.
7. Xiao SP, Belytscho T. A bridging domain method for coupling continua with molecular dynamics. *Computer Methods in Applied Mechanics and Engineering* 2004; **193**(17–20):1645–1669.
8. Abraham FF, Broughton JQ, Bernstein N, Kaxiras E. Spanning the length scales in dynamic simulation. *Computers in Physics* 1999; **12**(6):538–546.
9. Broughton JQ, Abraham FF, Bernstein N, Kaxiras E. Concurrent coupling of length scales: methodology and application. *Physical Review B* 1999; **60**(4):2391–2403.
10. E W, Huang Z. A dynamic atomistic-continuum method for the simulation of crystalline materials. *Journal of Computational Physics* 2002; **182**(1):234–261.
11. Li X, E W. Multiscale modeling of the dynamics of solids at finite temperature. *Journal of the Mechanics and Physics of Solids* 2005; **53**:1650–1685.
12. Fish J, Chen W. Discrete-to-continuum bridging based on multigrid principles. *Computer Methods in Applied Mechanics and Engineering* 2004; **193**:1693–1711.
13. Shilkrot LE, Curtin WA, Miller RE. A coupled atomistic continuum model of defects in solids. *Journal of the Mechanics and Physics of Solids* 2002; **50**:2085–2106.
14. Shiari B, Miller RE, Curtin WA. Coupled atomistic/discrete dislocation simulations of nanoindentation at finite temperature. *Journal of Engineering Materials and Technology* 2005; **127**:358–368.
15. Oden JT, Prudhomme S, Romkes A, Bauman P. Multi-scale modeling of physical phenomena: adaptive control of models. *ICES Report Number 05-13*, 2005.
16. Zhou M. A new look at the atomic level virial stress: on continuum-molecular system equivalence. *Proceedings of the Royal Society of London A* 2003; **459**:2347–2392.
17. Zhou M. Thermomechanical continuum representation of atomistic deformation at arbitrary size scales. *Proceedings of the Royal Society A* 2005; **461**:3437–3472.
18. Zimmerman JA, Webb EB, Hoyt JJ, Jones RE, Klein PA, Bammann DJ. Calculation of stress in atomistic simulation. *Modelling and Simulations in Materials Science and Engineering* 2004; **12**:S319–S332.
19. Curtin WA, Miller RE. Atomistic/continuum coupling in computational materials science. *Modelling and Simulations in Materials Science and Engineering* 2003; **11**:R33–R68.
20. Liu WK, Karpov EG, Zhang S, Park HS. An introduction to computational nanomechanics and materials. *Computer Methods in Applied Mechanics and Engineering* 2004; **193**(17–20):1529–1578.
21. Liu WK, Karpov EG, Park HS. *Nano Mechanics and Materials*: *Theory*, *Multiple Scale Analysis*, *and Applications* (1st edn). Wiley: Chichester, 2005.
22. Wagner GJ, Liu WK. Coupling of atomistic and continuum simulations using a bridging scale decomposition. *Journal of Computational Physics* 2003; **190**:249–274.
23. Tang S, Hou T, Liu WK. A mathematical framework of the bridging scale method. *International Journal for Numerical Methods in Engineering* 2006; **65**(10):1688–1713.
24. Park HS *et al*. The bridging scale for two-dimensional atomistic/continuum coupling. *Philosophical Magazine* 2005; **85**(1):79–113.
25. Park HS *et al*. Three-dimensional bridging scale analysis of dynamic fracture. *Journal of Computational Physics* 2005; **207**:588–609.
26. Park HS, Karpov EG, Liu WK. A temperature equation for coupled atomistic/continuum simulations. *Computer Methods in Applied Mechanics and Engineering* 2004; **193**:1713–1732.
27. Park HS, Liu WK. An introduction and tutorial on multiple-scale analysis in solids. *Computer Methods in Applied Mechanics and Engineering* 2004; **193**:1733–1772.
28. Freund LB. *Dynamic Fracture Mechanics* (1st edn). Cambridge University Press: Cambridge, 1990.

DOI: 10.1002/nme

29. Rice JR, Lapusta N, Ranjith K. Rate and state dependent friction and the stability of sliding between elastically deformable solids. *Journal of the Mechanics and Physics of Solids* 2001; **49**:1865–1898.
30. Rosakis AJ, Samudrala O *et al*. Cracks faster than the shear wave speed. *Science* 1999; **284**(5418):1337–1340.
31. Hao S, Liu WK, Klein PA, Rosakis AJ. Modeling and simulation of intersonic crack growth. *International Journal of Solids and Structures* 2004; **41**:1773–1799.
32. Li S, Liu WK, Rosakis AJ, Belytshko T, Hao W. Meshfree Galerkin simulations of dynamic shear band propagation and failure mode transition. *International Journal of Solids and Structures* 2002; **39**:1213–1240.
33. Li S, Liu WK, Qian D, Guduru R, Rosakis AJ. Dynamic shear band propagation and micro-structure of adiabatic shear band. *Computer Methods in Applied Mechanics and Engineering* 2001; **191**(1–2):73–92.
34. Abraham FF, Gao H. How fast can cracks propagate? *Physical Review Letters* 2000; **84**(14):3113–3116.
35. Gao H, Huang Y, Abraham FF. Continuum and atomistic studies of intersonic crack propagation. *Journal of the Mechanics and Physics of Solids* 2001; **49**:2113–2132.
36. Park HS, Karpov EG, Liu WK. Non-reflecting boundary conditions for atomistic, continuum and coupled atomistic/continuum simulations. *International Journal for Numerical Methods in Engineering* 2005; **64**: 237–259.
37. Cai W, de Koning M, Bulatov V, Yip S. Minimizing boundary reflections in couple-domain simulations. *Physical Review Letters* 2000; **85**(15):3213–3216.
38. Adelman SA, Doll JD. Generalized Langevin equation approach for atom/solid-surface scattering: collinear atom/harmonic chain model. *Journal of Chemical Physics* 1974; **61**(10):4242–4245.
39. Doll JD, Myers LE, Adelman SA. Generalized Langevin equation approach for atom/solid-surface scattering: inelastic studies. *Journal of Chemical Physics* 1975; **63**(11):4908–4914.
40. Adelman SA, Doll JD. Generalized Langevin equation approach for atom/solid-surface scattering: general formulation for classical scattering of harmonic solids. *Journal of Chemical Physics* 1976; **64**(6):2375–2388.
41. Karpov EG, Park HS, Liu WK. A phonon heat bath approach for the atomistic and multiscale simulation of solids. *International Journal for Numerical Methods in Engineering* 2005, preprint.
42. Weeks TW. Numerical inversion of Laplace transforms using Laguerre functions. *Journal of the ACM* 1966; **13**:419–429.
43. Crump KS. Numerical inversion of Laplace transforms using a Fourier series approximation. *Journal of the ACM* 1978; **23**(1):89–96.
44. Born M, Huang K. *Dynamical Theories of Crystal Lattices*. Clarendon: Oxford, 1956.
45. Qian D, Wagner GJ, Liu WK. A multiscale projection method for the analysis of carbon nanotubes. *Computer Methods in Applied Mechanics and Engineering* 2004; **193**(17–20):1603–1632.
46. Tahoe Development Server. http://tahoe.ca.sandia.gov
47. Matlab THK Code. http://apollo.mech.northwestern.edu/dave/downloads/THKcode.m

DOI: 10.1002/nme